



PAPER • **OPEN ACCESS**

Simultaneous enhanced electrochemical and photoelectrochemical properties of α -Fe₂O₃/graphene by hydrogen annealing

To cite this article: Yanyue Liu *et al* 2020 *Mater. Res. Express* **7** 025032

View the [article online](#) for updates and enhancements.

You may also like

- [Large coercivity of 13 kOe in L1₀-ordered CoPt on Si/SiO₂ substrates by hydrogen annealing](#)

Ryo Toyama, Shiro Kawachi, Jun-ichi Yamaura *et al.*

- [Experimental evidence of trap level modulation in silicon nitride thin films by hydrogen annealing](#)

Harumi Seki, Yuuichi Kamimuta and Yuichiro Mitani

- [Few layer graphene synthesis via SiC decomposition at low temperature and low vacuum](#)

Emre Kayali, Elif Mercan, Ersin Emre Oren *et al.*



The
Electrochemical
Society

Advancing solid state &
electrochemical science & technology



DISCOVER
how sustainability
intersects with
electrochemistry & solid
state science research



Materials Research Express



PAPER

OPEN ACCESS

RECEIVED
18 October 2019

REVISED
1 January 2020

ACCEPTED FOR PUBLICATION
16 January 2020

PUBLISHED
17 February 2020

Original content from this work may be used under the terms of the [Creative Commons Attribution 4.0 licence](#).

Any further distribution of this work must maintain attribution to the author(s) and the title of the work, journal citation and DOI.



Simultaneous enhanced electrochemical and photoelectrochemical properties of α -Fe₂O₃/graphene by hydrogen annealing

Yanyue Liu, Dongfang Guo, Kai Wu, Jinhang Guo and Zijiong Li

School of Physics & Electronic Engineering, Zhengzhou University of Light Industry, Zhengzhou, 450002, People's Republic of China

E-mail: zijiongli@zzuli.edu.cn

Keywords: α -Fe₂O₃ nanoplates/graphene, hydrogenation, oxygen vacancy, electrochemical properties, photoelectrochemical

Abstract

Two-dimensional (2D) materials have attracted extensive attention in various fields due to their good flexibility, high specific surface area and fast ion transfer rate. Herein, the α -Fe₂O₃ nanoparticles/graphene composites have been prepared through a hydrothermal method, which is followed by hydrogen annealing to produce oxygen vacancies. Electrochemical properties and photoelectrochemical properties are investigated. The results present a high specific capacitance and the electrochemical properties are improved ascribing to the synergistic effect of graphene's large specific surface area and excellent electrical conductivity, as well as the pseudocapacitance of transition metal oxides. Moreover, it also promotes the photoelectric response performances in visible light. This work provides a basis for the development and application of transition metal oxide in electrochemical and photoelectric fields.

1. Introduction

In recent decades, the development and utilization of new energy has become a major research trend. The energy storage devices and photoelectric conversion devices have been widely studied to use for the need of energy storage and conversion [1–5]. Supercapacitors are one of the most promising candidates, which benefit from their high-power density, fast charging rate, long cycle life, environmental protection and safety. The electrode material have attracted extensive attentions as an important component of capacitors. However, it is difficult to apply high-performance matrix materials on a large scale because of low reserves and high production cost. Therefore, it is emergency and important to develop a low-cost and affordable electrode material to meet the need for electrochemical energy storage devices is desired.

Transition metal oxides are attractive electrode materials due to their excellent pseudocapacitive properties and photoelectrical properties, including TiO₂, ZnO, Fe₂O₃, V₂O₅, Co₃O₄, SnO₂, BiVO₄, and WO₃, etc [6–12]. Hematite (α -Fe₂O₃) is one of the most typical n-type semiconductor materials. According to its relatively high theoretical capacitance, variable oxidation states, the rich natural reserves, suitable working window, non-toxic, and narrow band-gap (2.1 eV), etc [6, 13–15], it is generally considered to have broad prospects in thermoelectricity, photoelectricity, energy storage, catalytic degradation and other fields [16–21]. Especially in energy storage, Fe₂O₃ has a broad application prospect as an anode material. Nevertheless, its large-scale application is severely limited because of the easy agglomeration of nanoparticles during synthesis, the lower electronic conductivity, indirect transitions (d → d type), and short hole diffusion distance [6, 22, 23]. To overcome these shortcomings, the combination of α -Fe₂O₃ and other materials to form composite material is considered as a potential direction through synergistic effects to obtain higher performance than single-component oxides, such as 0 dimension (0D: metal ion, metal oxide), 1 dimension (1D: carbon nanotubes, carbon fiber), and 2 dimension (2D: graphene) [13, 24–28]. As expected, the composite demonstrates superior performance compared with single α -Fe₂O₃.

Among them, the development of 2D nanomaterials has received a sharp increase in attention [29–34]. Represented by graphene is a single layer of carbon atoms, a hexagonal honeycomb structure made up of sp² hybrid orbitals [35, 36], which has a unique layered structure and excellent physical and chemical properties

[37–40]. Typically, graphene is often used in double-layer capacitors according to the adsorption/desorption mechanism. Unfortunately, several factors have limited its performance gains, such as the fact that the surface of a material is not easy soaked by the electrolyte; and the stronger van der Waals force between sheets is easily causing agglomeration of graphene sheets [41, 42]. Therefore, combining graphene with metal oxide particles to form spacers between the layers not only prevents the layers from stacking but also further improves their performance due to synergistic effects [36, 43–45]. Before that, it has been reported that different shapes of iron oxide and graphene compound, showing the expected excellent properties. Wang *et al* [46] prepared single-crystalline α -Fe₂O₃/rGO composite aerogel with a specific capacitance of up to 908 F g⁻¹ at a current density of 2 A g⁻¹. Wu *et al* [47] reported Fe₂O₃ on rGO nanosheets to obtained Fe₂O₃/graphene composite by a one-step hydrothermal method with a specific capacitance of 1083 F g⁻¹ at a current density of 2 A g⁻¹. Bin Xiang *et al* [48] synthesized 2D nanometer round α -Fe₂O₃/rGO composites with an excellent specific capacitance of 621.3 F g⁻¹ at 5 mV s⁻¹ and 533 F g⁻¹ at 1 A g⁻¹ by a simple and inexpensive hydrothermal process. These higher specific capacitance of the samples are due to the fact that the introduction of graphene into metal oxides can accelerate the electron migration rates, increase the active sites and reduces the agglomeration of the α -Fe₂O₃ nanoparticles [49].

Moreover, the defect structure of metal oxide materials has an important influence on its physical and chemical properties. The formation energy of oxygen vacancy is much lower and easier to achieve than that of metal atom vacancy. In addition, oxygen vacancy can promote electrochemical charge transfer by generating gap electron states, so it is an important condition for impurity diffusion and semiconducting in crystals [50–54, 55]. In general, oxygen vacancy formation usually requires reductive reagents, hydrogenation treatment, and high-temperature treatment. The induced defects will affect the geometric structure, electronic structure and chemical properties of metal oxides, thus affecting the properties of materials.

Herein, the synthesis of rGO/ α -Fe₂O₃ composite by hydrothermal method has good properties, which not only solves the agglomeration of α -Fe₂O₃ but also avoids the interlayer stacking of rGO. Moreover, the nanocomposites with oxygen vacancy were prepared by hydrogen annealing. As expected, these unique features endow rGO/ α -Fe₂O₃ composite a better crystal structure and a faster electron transfer rate, exhibiting an excellent electrochemical and photoelectric property.

2. Experience section

2.1. Preparation of GO

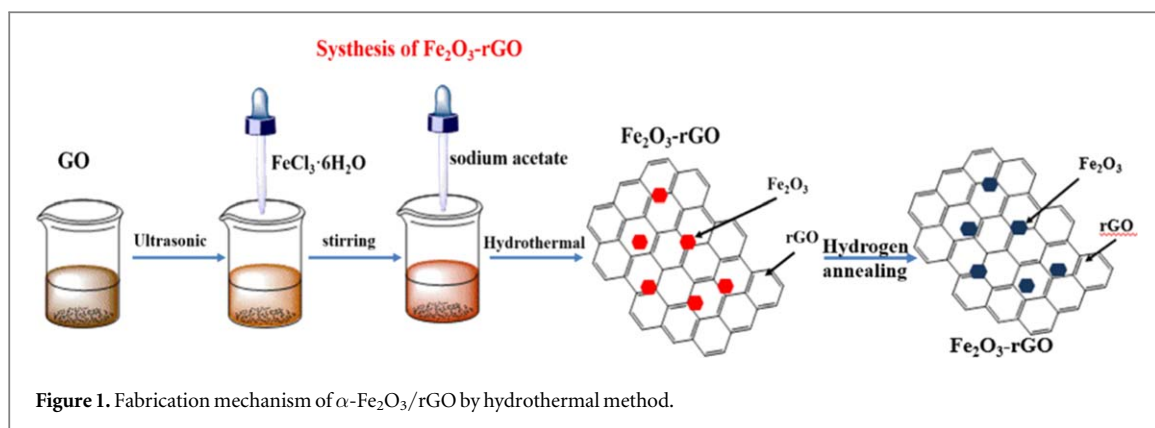
All the chemical reagents are analytical grade in the experiment and without further purification. The graphene (rGO) was exfoliated from natural graphite using a modified hummer method in this experiment. The experimental process is as follows: graphite powder (1.5 g) was immersed in a beaker with cold concentrated sulfuric acid (H₂SO₄) (50.7 ml). Then, sodium nitrate (1.14 g) was added to the mixture solution while stirring for 30 min. KMnO₄ (6 g) was added slowly while stirring for 2 h. After 3 days, 5% H₂SO₄ solution (150 ml) was slowly added and the reaction was finally terminated by the addition of 30% H₂O₂ (4.5 ml). After which the color of the solution change to bright yellow. 10% HCl (200 ml) was added to the mixture to remove the metal ions. Finally, the mixture was washed with plenty of deionized water until PH = 6, and then freeze-dry the precipitate to obtain GO.

2.2. Preparation of α -Fe₂O₃/rGO

The α -Fe₂O₃/graphene was synthesized by a one-step hydrothermal method. As shown in figure 1, GO (40 mg) was first added to ethanol (40 ml) and dispersed by ultrasound for 2 h. Then, 1.352 g FeCl₃·6H₂O was slowly added to the above GO solution, and a trace amount of deionized water was added and vigorously stirred for 30 min. Subsequently, add 4 g of sodium acetate while stirring and continue to stir for 1 h. After that, the mixed solution was transferred to the reaction kettle (100 mL) and the hydrothermal reaction was conducted for 24 h at 180 °C. After the solution was cooled to room temperature, it was centrifuge washed for 3–4 times with deionized water and ethanol, respectively. The collected precipitation was dried in vacuum at 60 °C for 10 h to obtain nanopowder of composite materials. The obtained sample was α -Fe₂O₃/rGO composite, denoted as GFC4. Other samples were prepared by the same process, with no GO added and with GO of different content (20 mg, 60 mg, 80 mg) denoted as Fe₂O₃, GFC2, GFC6, GFC8. In addition, GFC4 was treated by hydrogenated annealed for 3 h at 300 °C with a hydrogen ratio of 2%.

2.3. Characterization

The structure and morphology of the prepared α -Fe₂O₃ and its composites were characterized by x-ray diffraction (XRD) and field-emission scanning electron microscopy (FESEM, Quanta 250 FEG). XRD was used for the Bruker D8 Advance diffractometer with Cu K α radiation (λ = 1.5418 Å). The microstructure of the



samples was further characterized by transmission electron microscopy (TEM, JEOL JEM-2100). Nitrogen adsorption-desorption isotherms were obtained at 77 K using a micromeritics ASAP 2020 analyzer. The specific surface area (SBET) was evaluated using the Brunauer–Emmett–Teller (BET) method. Thermogravimetric analysis (TGA) was performed on SDT Q600 under N_2 from room temperature to 900 °C at 10 °C min⁻¹. X-ray photoelectron spectroscopic (XPS) was measured using a Thermo Scientific ESCALAB 250 Xi using Al K α radiation (USA). The UV–visible diffuse reflectance spectrums were measured by a UV–visible spectrophotometer.

2.4. Electrochemical performance test

The measuring system is a three-electrode measuring system, and the instrument used is an electrochemical workstation (Shanghai chenhua). The sample electrode was mixed evenly according to the proportion of active material 80%, conductive acetylene 10% and polytetrafluoroethylene (PTFE) 10%, and then anhydrous ethanol was added as a solvent to form a paste. Finally, it was uniformly applied on conductive foam nickel with an area of 1 cm². The electrode was dried in a vacuum drying box at 50 °C for 6 h and then press tightly with the tablet press to prevent the sample from falling off during the test. The electrode was immersed in the electrolyte for 8 h before the test. The prepared electrode was used as the working electrode, the reference electrode was a saturated calomel electrode, and the counter electrode was platinum plate. Electrochemical tests were performed in 6 mol KOH electrolyte solution, including cyclic voltammetry (CV), galvanostatic charge-discharge (GCD, voltage window from 0.2–0.6), and impedance spectra (EIS, 100 kHz to 0.01 Hz). The mass-specific capacitance is calculated by formula:

$$C = \frac{I\Delta t}{m\Delta V} \quad (1)$$

where I is the charge-discharge current, Δt is the discharge time, ΔV is voltage window, m is the mass of the active material.

2.5. Photoelectric performance test

The photoelectric properties of $\alpha\text{-Fe}_2\text{O}_3$ and other composite sample electrodes were tested on an electrochemical workstation using a xenon lamp (CHF-XM-500W) as a simulate of sunlight. The electrolyte was 0.1 M Na_2SO_4 aqueous solution. Each sample was sonically dissolved in an ethanol solvent at a concentration of 1 mg ml⁻¹, and then the same amount of solution was dripped through the pipette onto conductive glass (Indium tin oxide ITO) with an area of 1 cm². Finally, they were dried in a vacuum oven at 50 °C for 6 h, and the I-T curves and linear sweep voltammetry (LSV) were tested. The prepared electrode, platinum foil, and Hg/HgO were used as working, counter and reference electrodes, respectively.

3. Results and discussing

3.1. Structure and morphology analysis

The hydrothermal process of one-step preparation of $\alpha\text{-Fe}_2\text{O}_3/\text{rGO}$ composite materials is illustrated in figure 1. In the hydrothermal process, the Fe^{3+} cations from FeCl_3 react in solution to form FeOOH , which is attached to the surface of GO. Then, the hydrophilic functional groups on the surface of GO are partially removed during the reduction process, and GO is converted to rGO. After that, the FeOOH on the surface of rGO gradually decomposes into Fe_2O_3 [46]. Detailed steps are in the experiment section.

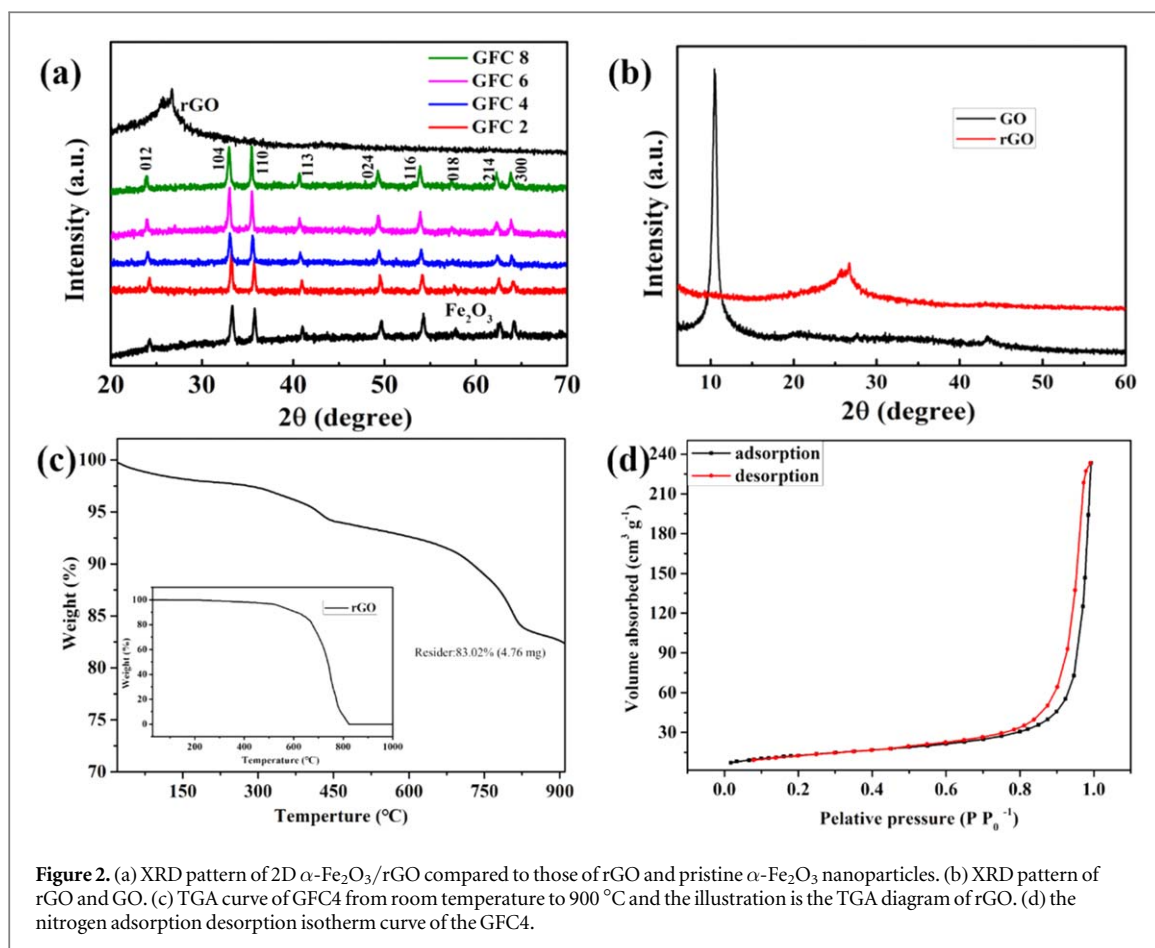


Figure 2. (a) XRD pattern of 2D α -Fe₂O₃/rGO compared to those of rGO and pristine α -Fe₂O₃ nanoparticles. (b) XRD pattern of rGO and GO. (c) TGA curve of GFC4 from room temperature to 900 °C and the illustration is the TGA diagram of rGO. (d) the nitrogen adsorption desorption isotherm curve of the GFC4.

XRD patterns of the structure and phase characteristics of 2D GFC, rGO and Fe₂O₃ are shown in figure 2(a). The result shows that no extra diffraction peaks of possible impurity compared with the pristine sample. All the diffraction peaks are consistent with the initial phase of α -Fe₂O₃ (space group: *R3c*), which corresponds well with the standard card (JCPDS no. 33–0664). This happens when the graphene lamellar structure collapses or is regularly distributed [56]. According to the analysis of the morphology of the corresponding samples, this phenomenon is caused by the high crystallization of α -Fe₂O₃ and the uniform dispersion on the surface of graphene. It is noteworthy that the peak (002) of graphene at the position of 26° indicates that GO can be reduced to rGO by hydrothermal reaction [57]. The XRD pattern from GO to rGO exhibits the GO has been successfully reduced (the right in figure 2(b)).

To determine the loading amount of Fe₂O₃ in the Fe₂O₃/rGO composites, TGA measurement of GO and GFC4 was carried out in air conditions (figure 2(c)). After the product had been calcined at 900 °C in air, the graphene content is shown in the illustration to be almost zero. It can be seen that the curve decline of the sample can be divided into two stages. The first stage is due to the absorbed water and impurities, and the second stage is the mass loss of graphene. The content of Fe₂O₃ in Fe₂O₃/rGO composites was calculated to be 83.02%. In addition, the specific surface area of the GFC4 samples are characterized by nitrogen adsorption-desorption isotherms measurements. As shown in figure 2(d), the typical type-IV isotherm of GFC4 indicates the presence of mesoporous structures. The BET specific surface area of GFC4 is larger than Fe₂O₃ powder values in the references [46, 58, 59]. This result demonstrates the advantages of the present rGO decorated route to produce large accessible surface area and prevent the restacking of graphene sheets.

Figure 3 shows the morphologies and sizes of the α -Fe₂O₃ and its composites characterized by FESEM. It can be seen from figure 3(a) that α -Fe₂O₃ shows a hexagonal structure of uniform size. The high magnification image of α -Fe₂O₃/rGO composite indicates that the α -Fe₂O₃ is firmly confined to the rGO nanosheet, with an average size of about 50–60 nm and evenly distributed. This prevents the agglomeration of α -Fe₂O₃ itself and the stacking between the rGO layers. In addition, the dispersion of α -Fe₂O₃ nanoparticles on rGO becomes more and more sparse with the increases of rGO content (figures 3(b)–(e)), which may have a certain influence on the performance of the electrode. In figure 4(a), the microstructure of the GFC4 after hydrogen annealing shows no significantly change. Furthermore, the microstructure of the GFC 4 after hydrogenation is employed by TEM. Typical regular lattice fringes in the selected region are shown in figure 4(b), and the d-spacing is 0.57 nm, corresponding to the d spacing of (110) planes [46].

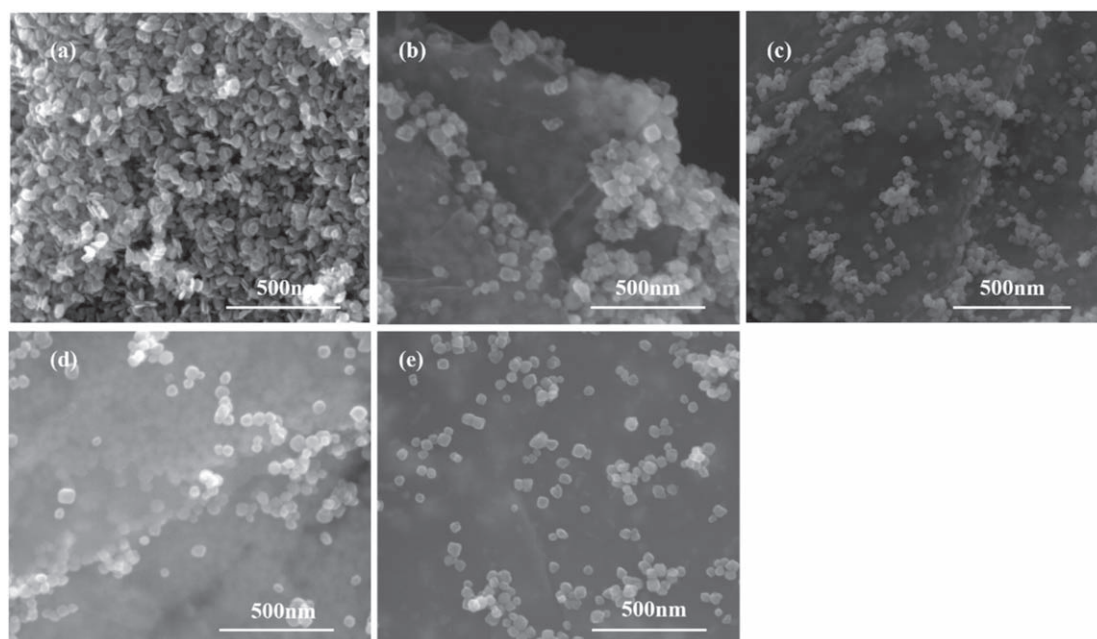


Figure 3. The SEM images of (a) α -Fe₂O₃, (b) GFC2, (c) GFC4, (d) GFC6, (e) GFC8 samples.

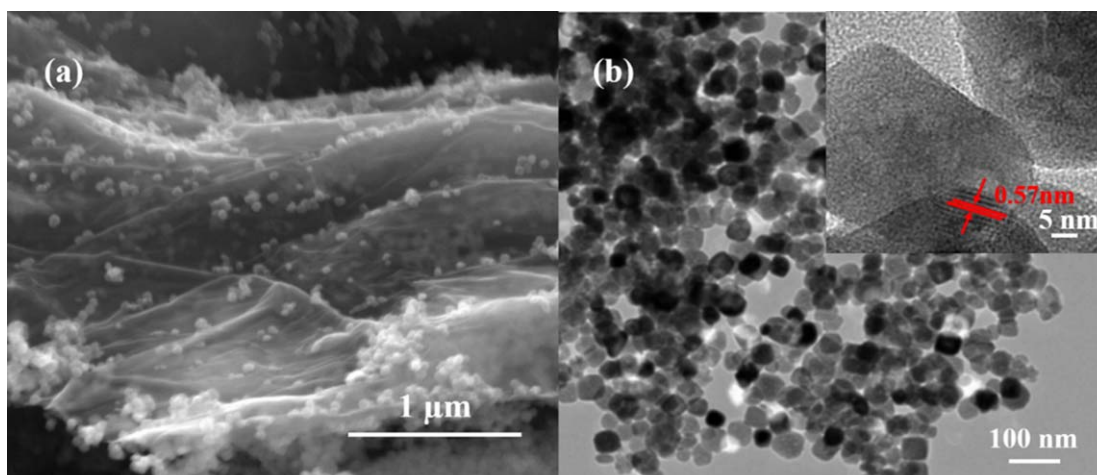


Figure 4. (a) SEM and (b) TEM image of GFC4 after hydrogenation.

The oxygen vacancies in semiconductor play key roles in promoting photoelectricity activity. X-ray photoelectron spectroscopy (XPS) characterization was applied to reveal the valence of cations and the existence of oxygen vacancies on GFC 4 before and after hydrogen annealing, respectively. The Fe atom has a doublet spectrum corresponding to Fe 2p_{3/2} and Fe 2p_{1/2} states as shown in figures 5(a), (c). The 2p_{3/2} spectra of Fe atom can be described as the superposition of two peaks by Gaussian distribution, which refers to the co-existence of both Fe³⁺ and Fe²⁺ ions of binding energies 711.4 and 710.7 eV, respectively[52, 60]. Meanwhile, the O 1s spectra (figures 5(b), (d)) can be divided into two characteristic peaks of Fe–O (530.2 eV O_I), defect sites with a low oxygen coordination (531.6 eV O_{II}) [61]. The higher O_{II} value of GFC4 after hydrogen annealing indicated that the composite possessed more oxygen vacancies [54].



Equations (1) and (2) show that the oxygen vacancies are responsible to create conduction electrons, and equation (3) shows the multivalent Fe-ions also could be key the factor to promote conduction process [60].

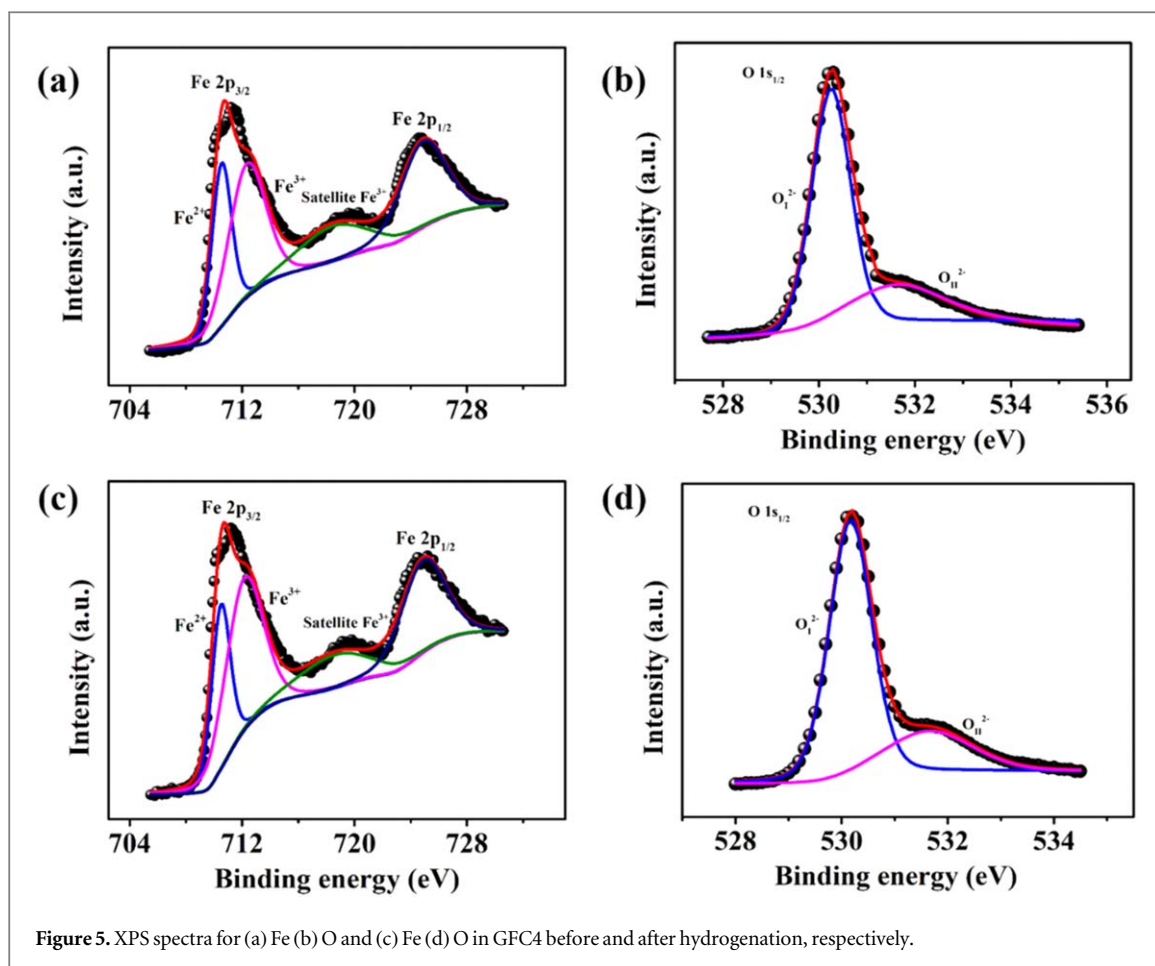
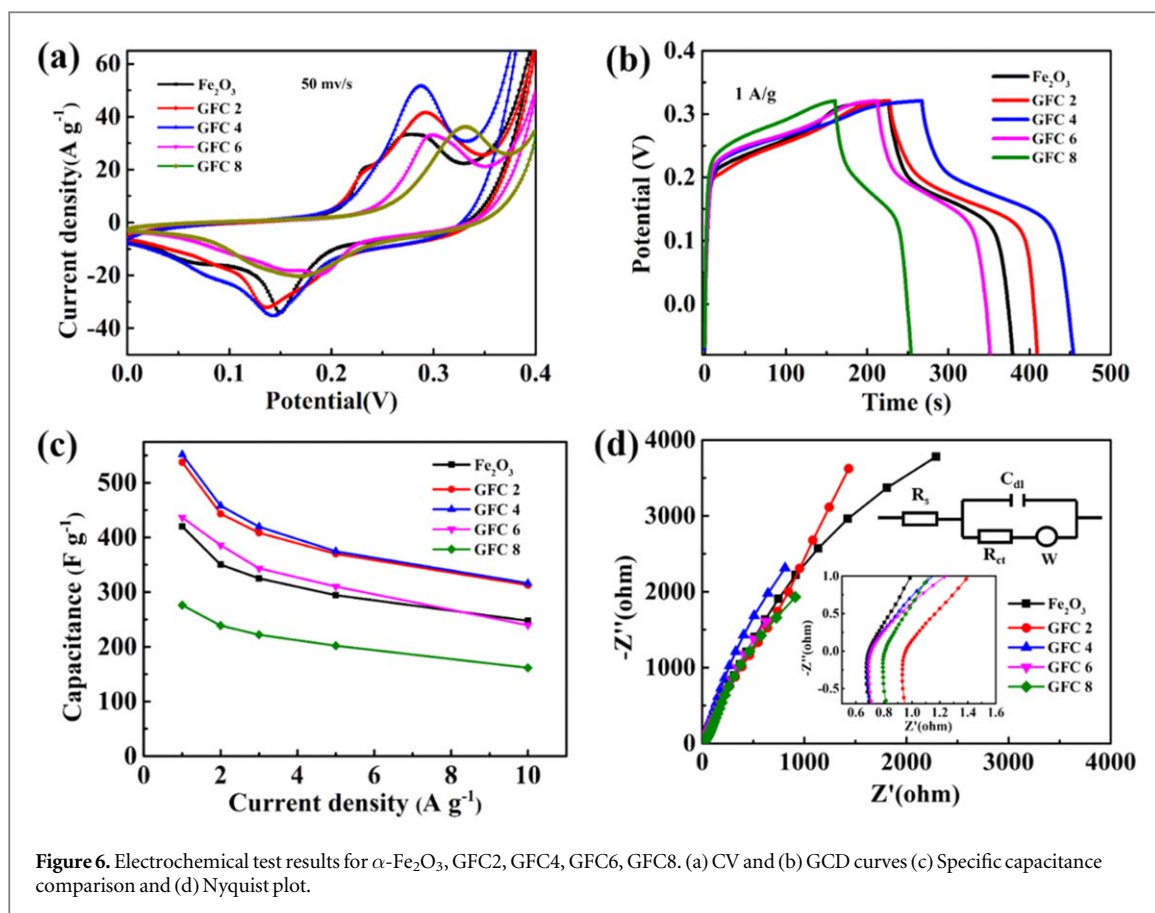


Figure 5. XPS spectra for (a) Fe (b) O and (c) Fe (d) O in GFC4 before and after hydrogenation, respectively.

3.2. Electrochemical properties

The electrochemical properties of sample electrodes with α -Fe₂O₃ and its different graphene composite proportions are measured in the three-electrode system. The comparison of CV curves at a scan rate of 50 mV s⁻¹ are plotted in figure 6(a). It can be seen that all the samples show a pair of obvious redox peaks, indicating that the charge storage mechanism of the electrode belongs to the Faraday battery generated by the valence state change of Fe²⁺/Fe³⁺. Among them, the area enclosed by the CV curve of electrode GFC4 is largest, which indicates that the electrode has the highest specific capacitance. It reveals that adding the appropriate amount of graphene can increase the storage performance of the material, which takes advantage of the synergistic effect between the pseudo-capacitance property of α -Fe₂O₃ and the double-layer properties of rGO. The GCD curves of the different samples electrode at the current density of 1 A g⁻¹ are shown in figure 6(b). According to the calculation of formula (1), the specific capacitance of the electrode are 420, 537.4, 551.5, 436.6 and 276.1 F g⁻¹ (corresponding to α -Fe₂O₃, GFC2, GFC4, GFC6, GFC8), respectively. Meanwhile, the rate properties of the electrode at different current densities (1, 2, 3, 5, 10 A g⁻¹) indicate that the composite materials have better overall specific capacitance when doped with a small amount of graphene, but the performance will decline when the excess is added. This is because excess graphene can lead to a re-stacking between the sheets, reducing the pore structure and surface area. The results show that the high concentration of rGO will affect the nanostructures of the material, which does not favor the diffusion of electrolyte in the hole and cannot provide a good channel for electrolyte ion conduction, and reduces the storage space of ions.

In addition, EIS characterization was used to deeper understand the electrodynamics of the electrode material, and the Nyquist plots of each sample are shown in figure 6(d). The illustration is an electrochemical equivalent circuit and a local magnification of the high frequency region. Where the distance of the curve from the origin on the X-axis represents the intrinsic resistance of the active material (R_s), and a smaller the intercept reveals a smaller resistance. The arc radius of the high-frequency region represents the sum of the contact resistance between the active material and the collector and the charge transfer contact resistance (R_{ct}) between the electrode and electrolyte. The low-frequency region is the resistance of ion movement from the electrolyte to the electrode/electrolyte interface, which is the Warburg impedance (W_0) caused by ion diffusion [62], and a larger the slope of the line represents a smaller W_0 . Therefore, the GFC4 electrode has relatively small resistance and high conductivity. The results demonstrates that adding appropriate amount of graphene can promote the



utilization rate and reaction kinetics of the active substances, and is beneficial to improve the performance of electrode material.

Figure 7 shows the comparison of electrochemical properties of α -Fe₂O₃, GFC4 and GFC4 after hydrogen annealing. It is worth noting that hydrotreating does not significantly promote the discharge time of the electrode at low current density. (figures 7(a)–(b)). However, the specific capacitance of GFC4 at high current density is improved compared with that before hydrogenation (figure 7(c)), and the clearer values are shown in table 1. Meanwhile, the cyclic stability tests of 8000 times at 10 A g⁻¹ also indicates that hydrogenation annealing improved the stability of the material and had superior performance (figure 7(d)). This result is attributed to the faster diffusion rate of the ion after hydrogen annealing, due to its higher crystallinity, and the formation of oxygen vacancy. Figures 7(e)–(f) shows the CV and GCD curves of GFC4 after hydrogen annealing electrode at different scanning rates. The shapes change of the curves in the figure is not obvious, which indicates that the electrode material has good stability and reversibility. Therefore, the α -Fe₂O₃/rGO composite can provide superior electrochemical performance. It can be inferred that the photoelectric response performance of the sample will increase after hydrogen annealing.

3.3. The photoelectrochemical performance

Considering that the semiconductor properties of Fe₂O₃ are more sensitive to light, the photoelectric properties of samples were studied under the light in 0.5 M Na₂SO₄. Figure 8(a) presents a typical transient current diagram (I-T) under chopped illumination, which shows a good switching behavior and uniform response when the lights are on and off. It shows the photocurrent of the GFC4 is highest than the pristine α -Fe₂O₃, and other composites. Furthermore, the linear sweep voltammetry (LSV) curves at voltage from -1.75 to 0 V for the rGO/ α -Fe₂O₃ composites and that of the pristine α -Fe₂O₃ are shown in figure 8(b). The results show that the electrical rectification behavior of samples is obviously, and the performance improvement is consistent with the trend of I-T.

Figure 9(a) shows the impedance spectrum of the samples before and after hydrogen annealing. The resistance of the sample is decreased after hydrotreatment. This provides a good basis for the improvement of photoelectric performance. The test results in figures 9(c)–(d) verify the improvement of conductivity and confirm the relationship between defect and photoelectric performance. The UV-vis diffuse reflectance spectra show the absorption of light from α -Fe₂O₃, GFC4 and GFC4 samples after hydrogen annealing. It is well known that semiconductors have a wide band, and the threshold is set according to its bandgap. The absorption

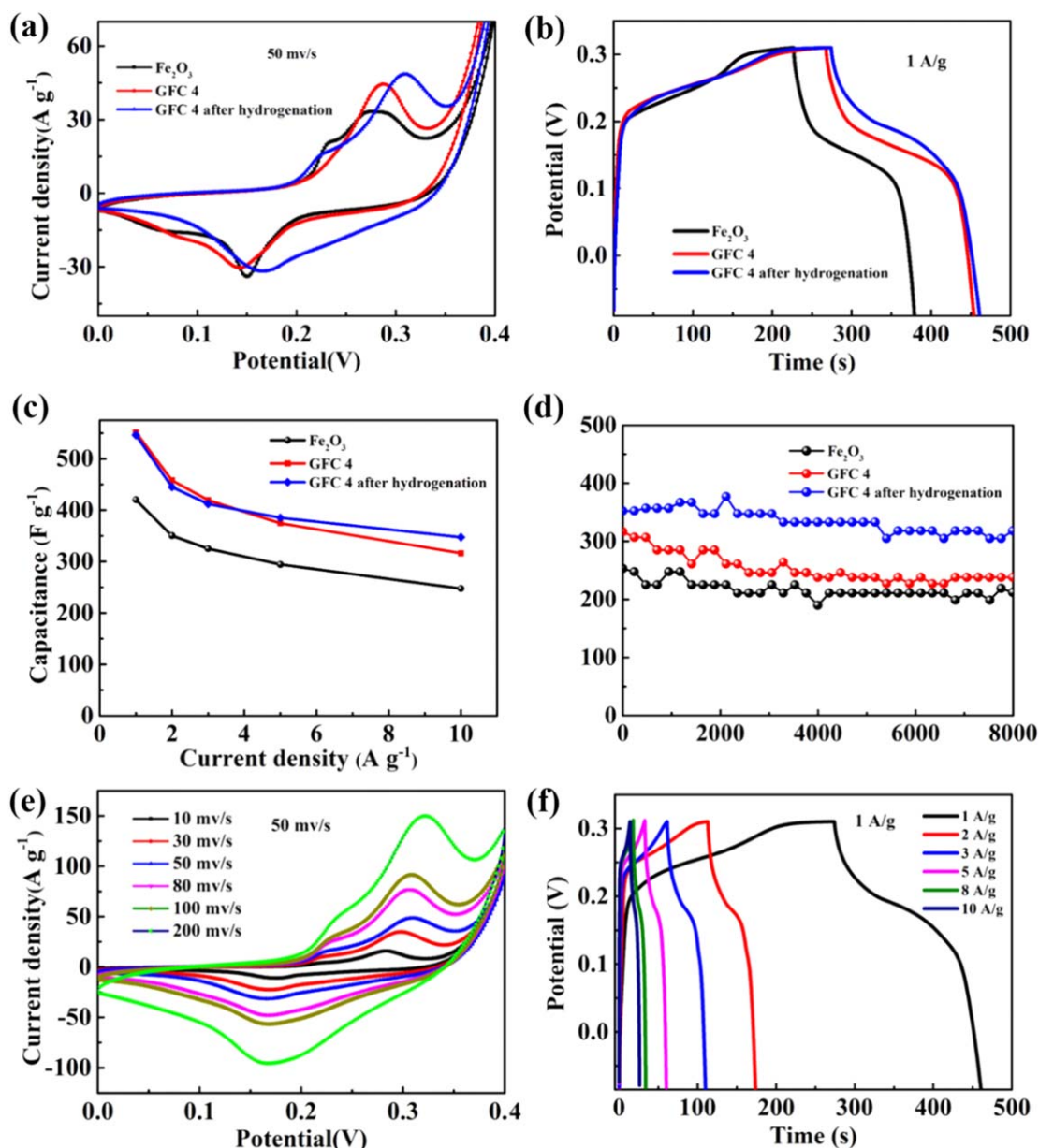


Figure 7. Electrochemical test results for $\alpha\text{-Fe}_2\text{O}_3$, GFC4, GFC4 after hydrogen annealing. (a) CV curves and (b) GCD curves, (c) Specific capacitance comparison and (d) Cycling stability performance at 10 A/g. (e) CV curves at different scanning rates (f) GCD curves at different current density of GFC4 after hydrogen annealing.

Table 1. Specific capacitance (F/g) comparison at different current density of GFC4 after hydrogen annealing.

Samples	1 A/g	2 A/g	3 A/g	5 A/g	10 A/g
$\alpha\text{-Fe}_2\text{O}_3$	420.2	350.35	325.05	294.25	247.5
GFC ₄	551.532	457.84	419.84	374.65	316.24
GFC ₄ after hydrogen annealing	546.1	445	412	385.1	347.3

threshold of $\alpha\text{-Fe}_2\text{O}_3$ is about 590 nm, and the absorption threshold of the sample formed after recombination with graphene in figure 9(b) is about 600 nm, which is consistent with the bandgap of $\alpha\text{-Fe}_2\text{O}_3$. However, due to the zero-band gap of graphene, the absorption intensity of composite in the visible region increases significantly. This is because the electron transfer between the energy bands of the composite nanocrystals and the oxygen

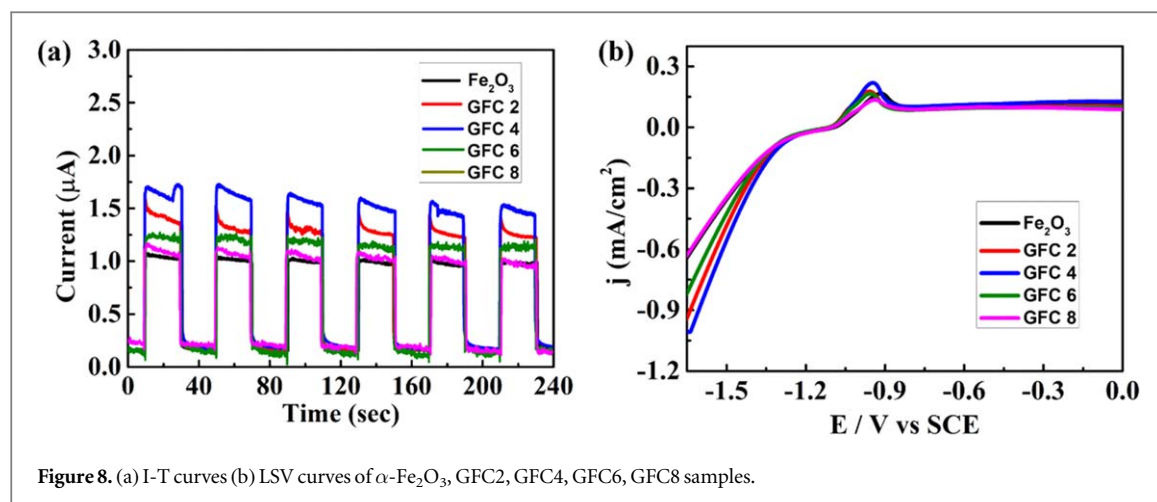


Figure 8. (a) I-T curves (b) LSV curves of α -Fe₂O₃, GFC2, GFC4, GFC6, GFC8 samples.

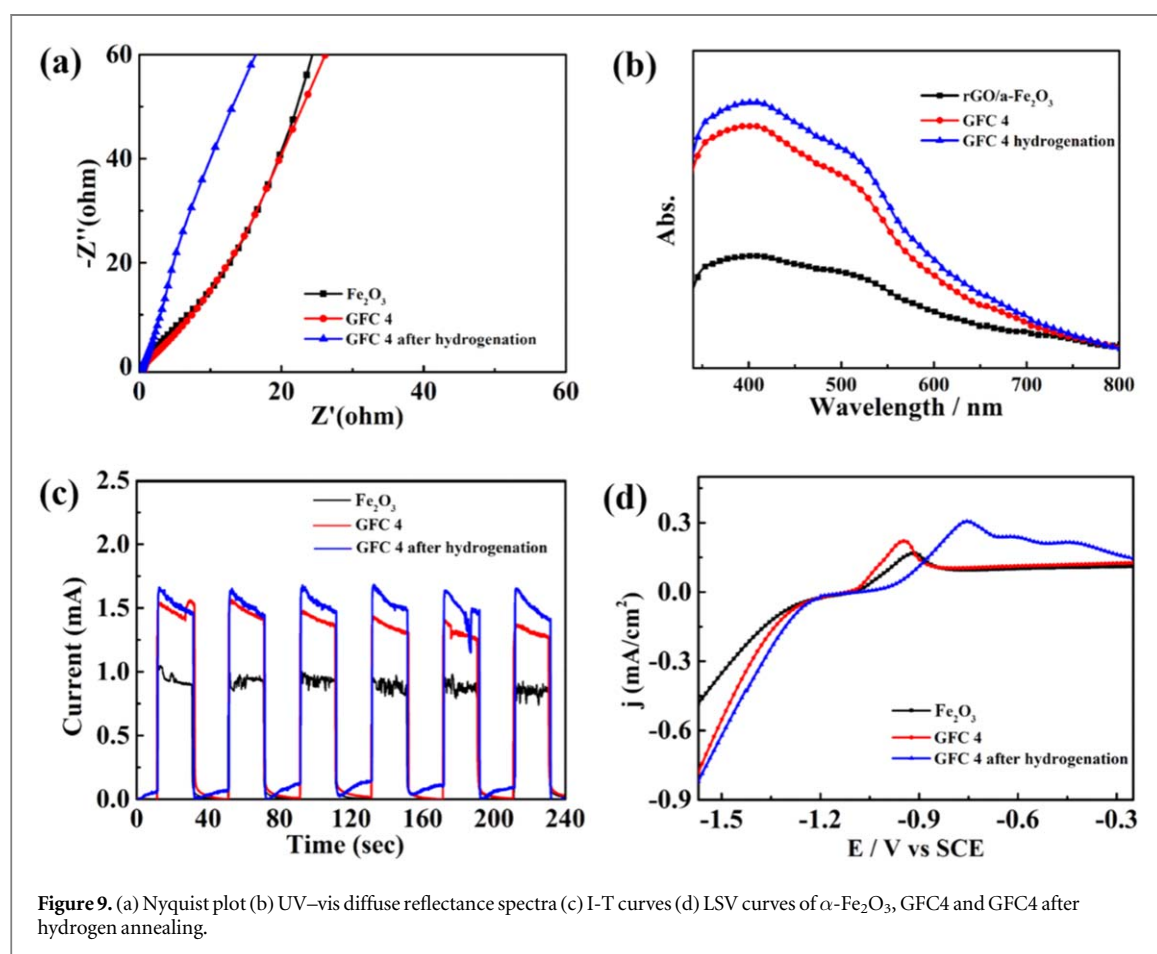
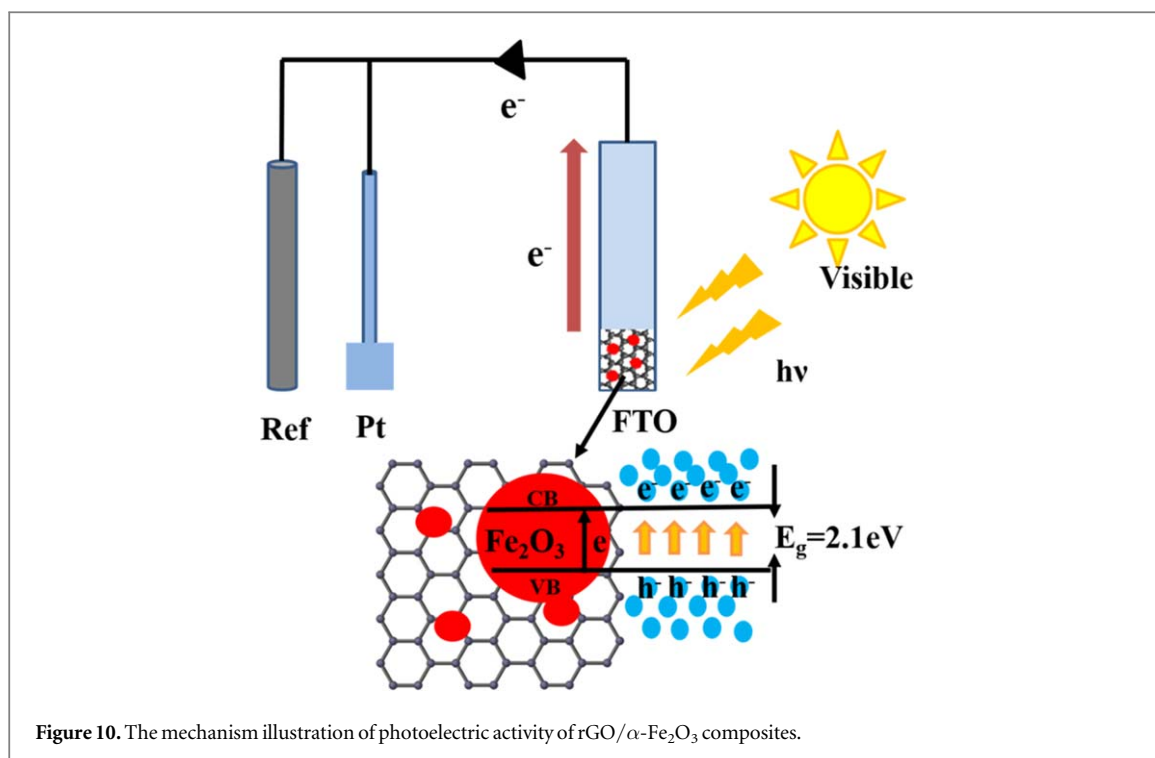


Figure 9. (a) Nyquist plot (b) UV-vis diffuse reflectance spectra (c) I-T curves (d) LSV curves of α -Fe₂O₃, GFC4 and GFC4 after hydrogen annealing.

vacancy generated internally change the electron density in the crystals, ensuring good electron and ion transport mechanics.

The complex theoretical mechanism of the electron-hole migration theory of rGO/ α -Fe₂O₃ complex under illumination is discussed in figure 10. According to early reports, the conduction band-edge (E_c) and valance band-edge (E_v) of Fe₂O₃ are -4.78 eV and -6.88 eV, respectively, and the band-gap width is 2.1 eV [6, 8]. Thus, charge separation cannot be carried out by the formula if the wavelength is lower than the 590 nm threshold ($E_g = hc/\lambda_{\max}$, $h = 4.13567 \times 10^{-15}$ eV s, $c = 3 \times 10^{17}$ nm s⁻¹). The electron-hole recombination rate of single Fe₂O₃ is high, while the graphene with high conductivity in the composite material can rapidly separate charge carriers and reduce the recombination rate. This is of great significance to the application of visible light in photoelectricity and energy production.



4. Conclusions

In summary, a series of the rGO/ α -Fe₂O₃ composite electrode materials are successfully prepared by controlling the mass of rGO in the hydrothermal process. The GFC4 sample exhibits an optimal electrochemical performance with a specific capacitance of 551.5 F g⁻¹ and has an excellent retention rate after 8,000 cycles with a current density of 10 A g⁻¹ in a three-electrode system. What's more, the oxygen vacancy generated by hydrogen annealing greatly improves the photoelectric response of the electrode. The improvement of these properties is mainly attributed to the combination of the large specific surface area and high conductivity of rGO, as well as the pseudo-capacitance of α -Fe₂O₃, and the generation of oxygen vacancies further facilitates the conductance process. This study provides a promising alternative strategy to develop excellent electrochemical and photoelectrochemical electrodes for energy storage devices.

Acknowledgments

The authors are grateful for support from the Henan Provincial Department of Education (No.17A140013), the Graduate's Scientific Research Foundation of Zhengzhou University of Light Industry (2018008), the science and technology project in Henan Province (No.202102210057).

Conflict of Interest

The authors declare no conflict of interest.

ORCID iDs

Zijiong Li  <https://orcid.org/0000-0002-8331-2522>

References

- [1] Sivula D K, Formal F L and Grätzel P D M 2011 Solar water splitting: progress using hematite (α -Fe₂O₃) photoelectrodes *ChemSusChem* **4** 432–49
- [2] Hagfeldt A, Boschloo G, Sun L, Kloo L and Pettersson H 2010 Dye-sensitized solar cells *Chem. Rev.* **110** 6595–663
- [3] Li J and Wu N 2015 Semiconductor-based photocatalysts and photoelectrochemical cells for solar fuel generation: a review *Catal. Sci. Technol.* **5** 1360
- [4] Liu C, Li F, Ma L P and Cheng H M 2010 Advanced materials for energy storage *Adv. Mater.* **22** E28–62

- [5] Chu S and Majumdar A 2012 Opportunities and challenges for a sustainable energy future *Nature* **488** 294–303
- [6] Lee W J, Shinde P S, Go G H and Doh C H 2014 Cathodic shift and improved photocurrent performance of cost-effective Fe_2O_3 photoanodes *Int. J. Hydrogen Energy* **39** 5575–9
- [7] Tian H, Wan C, Xue X, Hu X and Wang X 2017 Effective electron transfer pathway of the ternary $\text{TiO}_2/\text{RGO}/\text{Ag}$ nanocomposite with enhanced photocatalytic activity under visible light *Catalysts* **7** 156
- [8] Song X-M, Zhou X, Yuan C, Zhang* Y, Tong Q, Li Y, Cui L, Liu D and Zhang W 2017 One-dimensional $\text{Fe}_2\text{O}_3/\text{TiO}_2$ photoelectrode and investigation of its photoelectric properties in photoelectrochemical cell *Appl. Surf. Sci.* **397** 112–8
- [9] Liu Y, Wang D-P, Yu* Y-X and Zhang W-D 2012 Preparation and photoelectrochemical properties of functional carbon nanotubes and Ti co-doped Fe_2O_3 thin films *Int. J. Hydrogen Energy* **37** 9566–75
- [10] Yang J, Shi Q, Zhang R, Xie M, Jiang X, Wang F, Cheng X and Han W 2018 BiVO_4 quantum tubes loaded on reduced graphene oxide aerogel as efficient photocatalyst for gaseous formaldehyde degradation *Carbon* **138** 118–24
- [11] Yaw C S, Ruan Q, Tang J, Soh A K and Chong M N 2019 A Type II n-n staggered orthorhombic $\text{V}_2\text{O}_5/\text{monoclinic clinobisvanite BiVO}_4$ heterojunction photoanode for photoelectrochemical water oxidation: fabrication, characterisation and experimental validation *Chem. Eng. J.* **364** 177–85
- [12] Humayun M, Sun N, Raziq F, Zhang X, Yan R, Li Z, Qu Y and Jing L 2018 Synthesis of ZnO/Bi -doped porous LaFeO_3 nanocomposites as highly efficient nano-photocatalysts dependent on the enhanced utilization of visible-light-excited electrons *Appl. Catal. B: Environ.* **231** 23–33
- [13] Cui J and Pei Y 2019 Enhanced photocathodic protection performance of $\text{Fe}_2\text{O}_3/\text{TiO}_2$ heterojunction for carbon steel under simulated solar light *J. Alloy. Compd.* **779** 183–92
- [14] Banisharif A, Khodadadi A A, Mortazavi Y, Firooz A A, Beheshtian J, Agah S and Menbari S 2015 Highly active Fe_2O_3 -doped TiO_2 photocatalyst for degradation of trichloroethylene in air under UV and visible light irradiation: Experimental and computational studies *Appl. Catal. B: Environ.* **165** 209–21
- [15] Yao K, Basnet P, Sessions H, Larsen G K, Murph S E H and Zhao Y 2016 $\text{Fe}_2\text{O}_3\text{--TiO}_2$ core-shell nanorod arrays for visible light photocatalytic applications *Catal. Today* **270** 51–8
- [16] Dotan H, Kfir O, Sharlin E, Blank O, Gross M, Dumchin I, Ankonina G and Rothschild A 2013 Resonant light trapping in ultrathin films for water splitting *Nat. Mater.* **12** 158–64
- [17] Mansour H, Letifi H, Bargougui R, Almeida-Didry S D, Negulescu B, Autret-Lambert C, Gadri A and Ammar S 2017 Structural, optical, magnetic and electrical properties of hematite ($\alpha\text{-Fe}_2\text{O}_3$) nanoparticles synthesized by two methods: polyol and precipitation *Appl. Phys. A* **787**
- [18] Chen J and Gou L X W L X 2005 $\alpha\text{-Fe}_2\text{O}_3$ nanotubes in gas sensor and lithium-ion battery applications *Adv. Mater.* **17** 582–6
- [19] Wang G, Ling Y, Wheeler D A, George K E, Horsley K, Heske C, Zhang J Z and Li Y 2011 Facile synthesis of highly photoactive $\alpha\text{-Fe}_2\text{O}_3$ -based films for water oxidation *Nano Lett.* **11** 3503–9
- [20] Wahajuddin S A 2012 Superparamagnetic iron oxide nanoparticles: magnetic nanoplateforms as drug carriers *Int J Nanomedicine* **7** 3445–71
- [21] Zhong L S, Hu J S, Liang H P, Cao A M, Song W G and Wan L J 2006 Self-assembled 3D flowerlike iron oxide nanostructures and their application in water treatment *Adv. Mater.* **18** 2426–31
- [22] Dare-Edwards M P, Goodenough J B, Andrew H and Trelvellick P R 1983 Electrochemistry and photoelectrochemistry of iron(III) oxide *J. Chem. Soc. Faraday Trans.* **79** 2027–41
- [23] Cherepy N J, Liston D B, Lovejoy J A, Deng H and Zhang J Z 1998 Ultrafast studies of photoexcited electron dynamics in c- and $\text{r-Fe}_2\text{O}_3$ semiconductor nanoparticles *J. Phys. Chem. B* **102** 770–6
- [24] Sivula K, Formal F L and Grätzel M 2009 $\text{WO}_3\text{--Fe}_2\text{O}_3$ Photoanodes for Water Splitting: a Host Scaffold, Guest Absorber Approach *Chem. Mater.* **21** 2862–7
- [25] Wang Z, Luan D, Madhavi S, Hu Y and Lou X W 2012 Assembling carbon-coated $\alpha\text{-Fe}_2\text{O}_3$ hollow nanohorns on the CNT backbone for superior lithium storage capability *Energy Environ. Sci.* **5** 5252–6
- [26] Xia G, Li N, Li D, Liu R, Wang C, Li Q, Lu X, Spendlow J S, Zhang J and Wu G 2013 Graphene/ $\text{Fe}_2\text{O}_3/\text{SnO}_2$ ternary nanocomposites as a high-performance anode for lithium ion batteries *ACS Appl. Mater. Interfaces* **5** 8607–14
- [27] Yang P, Ding Y, Lin Z, Chen Z, Li Y, Qiang P, Ebrahimi M, Mai W, Wong C P and Wang Z L 2014 Low-cost high-performance solid-state asymmetric supercapacitors based on MnO_2 nanowires and Fe_2O_3 nanotubes *Nano Lett.* **14** 731–6
- [28] Sun Z, Yuan H, Liu Z, Han B and Zhang X 2005 A highly efficient chemical sensor material for H_2S : $\alpha\text{-Fe}_2\text{O}_3$ nanotubes fabricated using carbon nanotube templates *Adv. Mater.* **17** 2993–7
- [29] Qiao Q, Liu C, Gao W and Huang L 2019 Graphene oxide model with desirable structural and chemical properties *Carbon* **143** 566–77
- [30] Gao W, Havas D, Gupta S, Pan Q, He N, Zhang H, Wang H-L and Wu G 2016 Is reduced graphene oxide favorable for nonprecious metal oxygen-reduction catalysts? *Carbon* **102** 346–56
- [31] Gao W, Majumder M, Alemany L B, Narayanan T N, Ibarra M A, Pradhan B K and Ajayan P M 2011 Engineered graphite oxide materials for application in water purification *ACS Appl. Mater. Interfaces* **3** 1821–6
- [32] Mahdavi M, Rahmania F and Nouranian S 2016 Molecular simulation of pH-dependent diffusion, loading, and release of doxorubicin in graphene and graphene oxide drug delivery systems *J. Mater. Chem. B* **4** 7441–51
- [33] Liu Q, Zhang M, Huang L, Li Y, Chen J, Li C and Shi* G 2015 High-quality graphene ribbons prepared from graphene oxide hydrogels and their application for strain sensors *ACS Nano* **9** 12320–6
- [34] Castro Neto A H, Guinea F, Peres N M R, Novoselov K S and Geim A K 2009 The electronic properties of graphene *Rev. Mod. Phys.* **81** 109–62
- [35] Dave S H, Gong C, Robertson A W, Warner J H and Grossman J C 2016 Chemistry and structure of graphene oxide via direct imaging *ACS Nano* **10** 7515–22
- [36] Stankovich S, Dikin D A, Dommett G H B, Kohlhaas K M, Zimney E J, Stach E A, Piner R D, Nguyen S T and Ruoff R S 2006 Graphene-based composite materials *Nature* **402** 282–6
- [37] Biswal S, Bhaskaram D and Govindaraj G 2018 Graphene oxide: structure and temperature dependent magnetic characterization *Mater. Res. Express* **5**
- [38] Zhu Y, Murali S, Cai W and Li X 2010 ChemInform abstract: graphene and graphene oxide: synthesis, properties, and applications *Adv. Mater.* **22** 3906–24
- [39] Chabot V, Higgins D, Yu A, Xiao X, Chen Z and Zhang J 2014 A review of graphene and graphene oxide sponge: material synthesis and applications to energy and the environment *Energ. Environ. Sci.* **7** 1564–96
- [40] Geim A K and Novoselov K S 2007 The rise of graphene *Nature Mater.* **6** 183–91

- [41] Zhang M, Zhao F, Yang Y, Zhang J, Li N and Gao H 2018 Effect of rGO-Fe₂O₃ nanocomposites fabricated in different solvents on the thermal decomposition properties of ammonium perchlorate *CrystEngComm* **20** 7010–9
- [42] Chabot V, Higgins D, Yu A, Xiao X, Chen Z and Zhang J 2014 A review of graphene and graphene oxide sponge: material synthesis and applications to energy and the environment, *Energ Environ. Sci.* **7** 1564–96
- [43] Kecsenovity E, Endrődi B Z, Tóth P T S, Zou Y, Dryfe R A W, Rajeshwar K and Janáky C 2017 Enhanced photoelectrochemical performance of cuprous oxide/graphene Nanohybrids *J. Am. Chem. Soc.* **139** 6682–92
- [44] Xiang Q, Yu J and Jaroniec M 2012 Graphene-based semiconductor photocatalysts *Chem. Soc. Rev.* **41** 782–96
- [45] Polfus J M, Løvvik O M, Rørvik P M and Bredeesen R 2016 Nanocomposites of few-layer graphene oxide and alumina by density functional theory calculations *J. Eur. Ceram. Soc.* **36** 719–24
- [46] Wang H, Xu Z, Yi H, Wei H, Guo Z and Wang X 2014 One-step preparation of single-crystalline Fe₂O₃ particles/graphene composite hydrogels as high performance anode materials for supercapacitors *Nano Energy* **7** 86–96
- [47] Gao Y, Wu D, Wang T, Jia D, Xia W, Lv Y, Cao Y, Tan Y and Liu P 2016 One-step solvothermal synthesis of quasi-hexagonal Fe₂O₃ nanoplates/graphene composite as high performance electrode material for supercapacitor *Electrochim. Acta* **191** 275–83
- [48] Zhu S, Zou X, Zhou Y, Zeng Y, Long Y, Yuan Z, Wu Q, Li M, Wang Y and Xiang B 2019 Hydrothermal synthesis of graphene-encapsulated 2D circular nanoplates of α -Fe₂O₃ towards enhanced electrochemical performance for supercapacitor *J. Alloy. Compd.* **775** 63–71
- [49] Dey A, Athar J and Varma P 2014 Graphene-iron oxide nanocomposite (GINC): an efficient catalyst for ammonium perchlorate (AP) decomposition and burn rate enhancer for AP based composite propellant *RSC Adv.* **5** 723–4
- [50] Wang G, Wang H, Ling Y, Tang Y, Yang X, Fitzmorris R C, Wang C, Zhang J Z and Li Y 2011 Hydrogen-treated TiO₂ nanowire arrays for photoelectrochemical water splitting *Nano Lett.* **11** 3026–33
- [51] Kim H S, Cook J B, Lin H, Ko J S, Tolbert S H, Ozolins V and Dunn B 2017 Oxygen vacancies enhance pseudocapacitive charge storage properties of MoO_{3-x} *Nat. Mater.* **16** 454–60
- [52] Wang J, Wang Z, Huang B, Ma Y, Liu Y, Qin X, Zhang X and Dai Y 2012 Oxygen vacancy induced band-gap narrowing and enhanced visible light photocatalytic activity of ZnO *ACS applied materials & interfaces* **4** 4024–30
- [53] Pan X, Yang M Q, Fu X, Zhang N and Xu Y J 2013 Defective TiO₂ with oxygen vacancies: synthesis, properties and photocatalytic applications *Nanoscale* **5** 3601–14
- [54] Zhuang L, Ge L, Yang Y, Li M, Jia Y, Yao X and Zhu Z 2017 Ultrathin iron-cobalt oxide nanosheets with abundant oxygen vacancies for the oxygen evolution reaction *Adv. Mater.* **29**
- [55] Yang S, Liu Y, Hao Y, Yang X, Goddard W A 3rd, Zhang X L and Cao B 2018 Oxygen-vacancy abundant ultrafine Co₃O₄/graphene composites for high-rate supercapacitor electrodes *Adv Sci (Weinh)* **5** 1700659
- [56] Sephra P J, Baraneedharan P, Sivakumar M, Thangadurai T D and Nehru K 2018 *In situ* growth of hexagonal-shaped α -Fe₂O₃ nanostructures over few layered graphene by hydrothermal method and their electrochemical performance *J. Mater. Sci. - Mater. El.* **29** 6898–908
- [57] Kaprants K, Mateuss J, Dorondo A, Bajars G, Kucinskis G, Lesnichenoks P and Kleperis J 2018 Electrophoretically deposited α -Fe₂O₃ and TiO₂ composite anchored on rGO with excellent cycle performance as anode for lithium ion batteries *Solid State Ionics* **319** 1–6
- [58] Zhang H, Lu C, Chen C, Xie L, Zhou P and Kong Q 2017 2D Layered α -Fe₂O₃/rGO flexible electrode prepared through colloidal electrostatic self-assembly *ChemElectroChem* **4** 1990–6
- [59] Li Z, Zhang W, Su Y, Li Z and Groeper J 2017 Self-assembling Ni(OH)₂/alpha-Fe₂O₃ composites for pseudocapacitors with excellent electrochemical performance *Nanotechnology* **28** 045603
- [60] Patri T, Justin P, Babu P D and Ghosh A 2019 Analysis of dielectric and magnetic phase transitions in Yb(Fe_{0.5}Cr_{0.5})O₃ bulk perovskite *Appl. Phys. A* **125**
- [61] Jo W K and Selvam N C 2015 Synthesis of GO supported Fe₂O₃-TiO₂ nanocomposites for enhanced visible-light photocatalytic applications *Dalton Trans.* **44** 16024–35
- [62] Cai Q, Zhang Y, Liang C, Li P, Gu H, Liu X, Wang J, Shentu Z, Fan J and Shao G 2018 Enhancing efficiency of planar structure perovskite solar cells using Sn-doped TiO₂ as electron transport layer at low temperature *Electrochim. Acta* **261** 227–35